

# First operation and performance of a 200 It double phase LAr LEM-TPC with a $40 \times 76 \text{ cm}^2$ readout

---

**A. Badertscher, A. Curioni, U. Degunda, L. Epprecht, A. Gendotti, S. Horikawa, L. Knecht, D. Lussi, G. Natterer, K. Nguyen, F. Resnati, A. Rubbia<sup>\*</sup>and T. Viant**

*ETH Zurich, Institute for Particle Physics,  
CH-8093 Zürich, Switzerland  
E-mail: Andre.Rubbia@cern.ch*

**ABSTRACT:** In this paper we describe the design, construction, and operation of a first large area double-phase liquid argon Large Electron Multiplier Time Projection Chamber (LAr LEM-TPC). The detector has a maximum drift length of 60 cm and the readout consists of a  $40 \times 76 \text{ cm}^2$  LEM and 2D projective anode to multiply and collect drifting charges. Scintillation light is detected by means of cryogenic PMTs positioned below the cathode. To record both charge and light signals, we have developed a compact acquisition system, which is scalable up to ton-scale detectors with thousands of charge readout channels. The acquisition system, as well as the design and the performance of custom-made charge sensitive preamplifiers, are described. The complete experimental setup has been operated for a first time during a period of four weeks at CERN in the cryostat of the ArDM experiment, which was equipped with liquid and gas argon purification systems. The detector, exposed to cosmic rays, recorded events with a single-channel signal-to-noise ratio in excess of 30 for minimum ionising particles. Cosmic muon tracks and their  $\delta$ -rays were used to assess the performance of the detector, and to estimate the liquid argon purity and the gain at different amplification fields.

**KEYWORDS:** liquid argon; double phase liquid argon TPC; charge sensitive preamplifier; readout; TPC; tracking chamber.

---

<sup>\*</sup>Corresponding author.

---

## Contents

<b>1. Introduction</b>	<b>1</b>
<b>2. The experimental setup</b>	<b>2</b>
2.1 The LAr LEM-TPC	3
2.2 The charge readout sandwich	4
<b>3. Readout electronics</b>	<b>6</b>
3.1 Design requirements	7
3.2 Charge sensitive preamplifiers	9
3.3 Data acquisition system	11
<b>4. First operation and performance of the LEM-TPC</b>	<b>13</b>
4.1 Detector commissioning and operation	13
4.2 Event reconstruction	14
4.3 Free electron lifetime measurement	17
4.4 Amplification gain and energy spectrum of $\delta$ -rays	18
<b>5. Conclusions</b>	<b>20</b>

---

## 1. Introduction

The liquid argon time projection chamber (LAr-TPC) [1] is a charge imaging detector which allows to reconstruct tracks in three dimensions as well as the deposited energy. In this context, the Giant Liquid Argon Charge Imaging ExpeRiment (GLACIER) is a concept proposed for a future observatory for neutrino physics and nucleon decay searches [2, 3, 4], which could be scalable up to gigantic masses of 100 kton. The key and innovative feature of the GLACIER design is the double phase LEM-TPC operation mode with adjustable gain and 2D projective readout [5, 6, 7]. The ionisation charge is extracted to the argon gas phase where it is amplified by a Large Electron Multiplier (LEM) which triggers Townsend multiplication in the high field regions in the LEM holes. The charge is collected and recorded on a two-dimensional and segmented anode. This principle has two main advantages: 1. the gain in the LEM is adjustable, i.e. the signal quality can be optimised, and 2. the signals collected on the two readout views are unipolar and symmetric which facilitates the event reconstruction. In addition to the ionisation charge, scintillation light is emitted by excited argon diatomic molecules (excimers). The detection of the scintillation light is fast, thus providing the event time reference  $T_0$ .

We have previously reported on the construction and successful operation of a  $10 \times 10 \text{ cm}^2$  LAr LEM TPC with 2D projective readout [5]. Following a staged approach, the next step towards

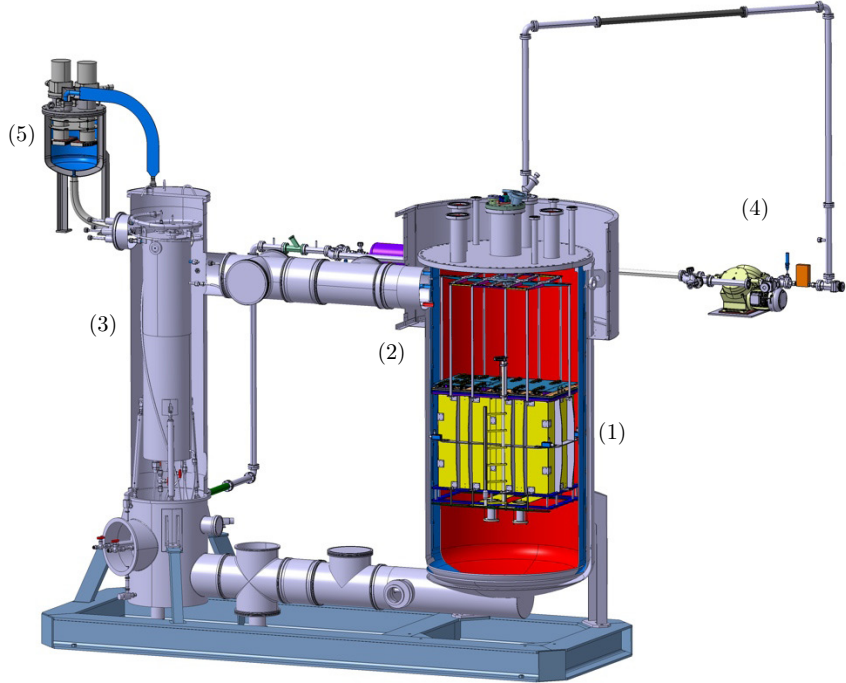


**Figure 1.** CAD drawing of the system. The detector (1) hanging from the top flange of the ArDM vessel (2), the liquid argon recirculation column (3) containing the custom made pump and filter, the gas recirculation system (4) and the re-condenser, with two cryocoolers (5).

large-area detectors was the construction of the so far largest singular unit of this kind, with a readout cross-section of  $40 \times 76 \text{ cm}^2$  (of a  $\sim 0.5 \text{ m}^2$  scale) and a drift of 60 cm, for a total volume of about 200 lt. The complete double phase readout system, henceforth referred to as *charge readout sandwich*, consists of two extraction grids, the LEM and a 2D anode, stacked on top of each other. It is a standalone structure that can be considered as basic module to cover larger surfaces of bigger detectors. After the production and assembly, the detector was successfully operated during one month inside the cryostat of the ArDM experiment operated on surface at CERN [8, 9, 10].

This paper is subdivided in four parts: in Section 2 we first describe the experimental setup and design and construction of the charge readout sandwich. Section 3 is about the design and the layout of the charge and light acquisition, including a detailed paragraph on the custom made charge sensitive preamplifiers. Finally, in Section 4 we report on the performance of the detector and the data acquisition system, which then leads to the conclusions in Section 5.

## 2. The experimental setup

The cryogenic setup developed for the ArDM experiment (See Figure 1) has been employed to provide the required thermodynamic stability and liquid argon purity for the double phase operation of the chamber. The ArDM cryogenic infrastructure consists of two main parts: the detector vessel, and the liquid argon cryogenic circuit for LAr purification and boil off recondensation. Both are surrounded by a separate volume that acts as external bath. The ArDM vessel is a vacuum tight cylindrical container (1 m in diameter and about 2 m high) connected to the liquid recirculation

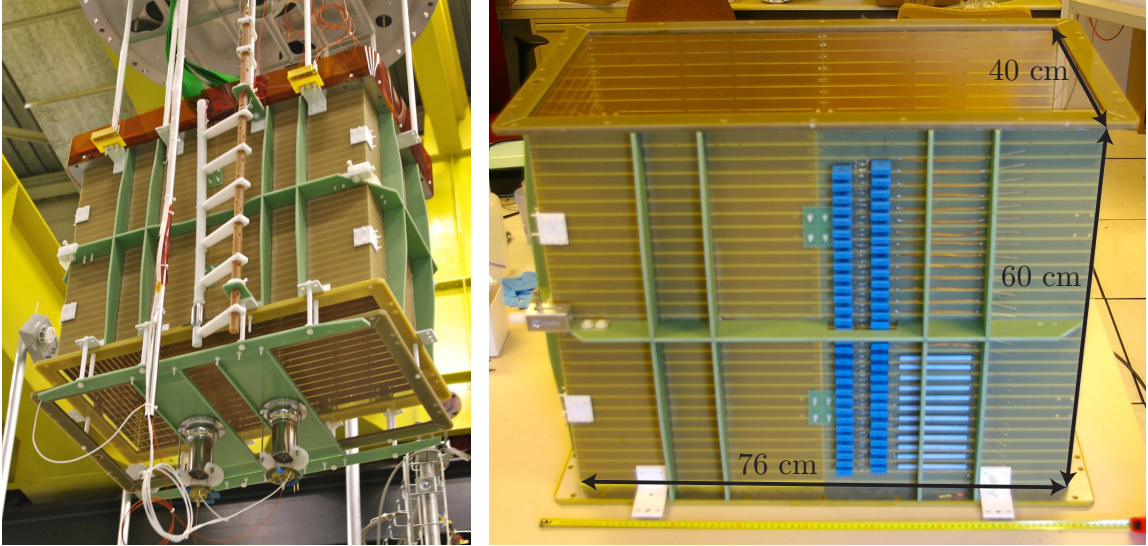


**Figure 2.** Pictures of the detector. Left: fully assembled detector hanging from the top flange of the ArDM vessel. Right: TPC during the assemblage phase.

column. Due to the large volume of liquid argon ( $\sim 1 \text{ m}^3$ ) that can be contained in the ArDM vessel, both liquid and gas purification are implemented. The liquid recirculation, consisting of a liquid pump and a purification cartridge, is custom made, while the gas recirculation employs commercial solutions for the pump and the cartridge. The thermodynamic conditions are controlled by two Gifford-McMahon cryocoolers<sup>1</sup>, that re-condense the boil off argon of the external bath. The cryocoolers are controlled by a Programmable Logic Control (PLC) unit, that also monitors all the slow control processes related to the pressures and temperatures of the system. The detector is hanging from the top flange of the vessel, as shown in Figure 2. Two 3 inch cryogenic PMTs<sup>2</sup> are installed below the cathode, protected by a metallic grid kept at ground. The window of one PMT was coated with Tetraphenyl Butadiene (TPB) in a polymer matrix in order to convert the scintillation light into visible light [11]. The primary scintillation signals are used as trigger for the charge readout.

## 2.1 The LAr LEM-TPC

The drift cage is made out of Printed-Circuit-Board (PCB) plates. As shown in Figure 3, it is limited on the bottom by the cathode grid and on the top by the extraction grids. It is 60 cm high and  $40 \times 76 \text{ cm}^2$  in cross section to match the dimensions of the readout sandwich. Thirty-one field shaping electrodes spaced 2 cm are printed with PCB techniques on the internal surfaces of the plates. They ensure the uniformity of the drift field along the entire volume. The high voltage for the drift field is provided by an immersed 30 stages Greinacher voltage multiplier circuit, also known as Cockcroft-Walton voltage multiplier. A more detailed description of the Greinacher voltage multiplier and its performance can be found elsewhere [8, 12]. The components are directly mounted on the external PCB wall completely immersed in the liquid (see Figure 2, right). The DC

<sup>1</sup>Air-cooled Cryomech AL 300.

<sup>2</sup>Hamamatsu R11065.

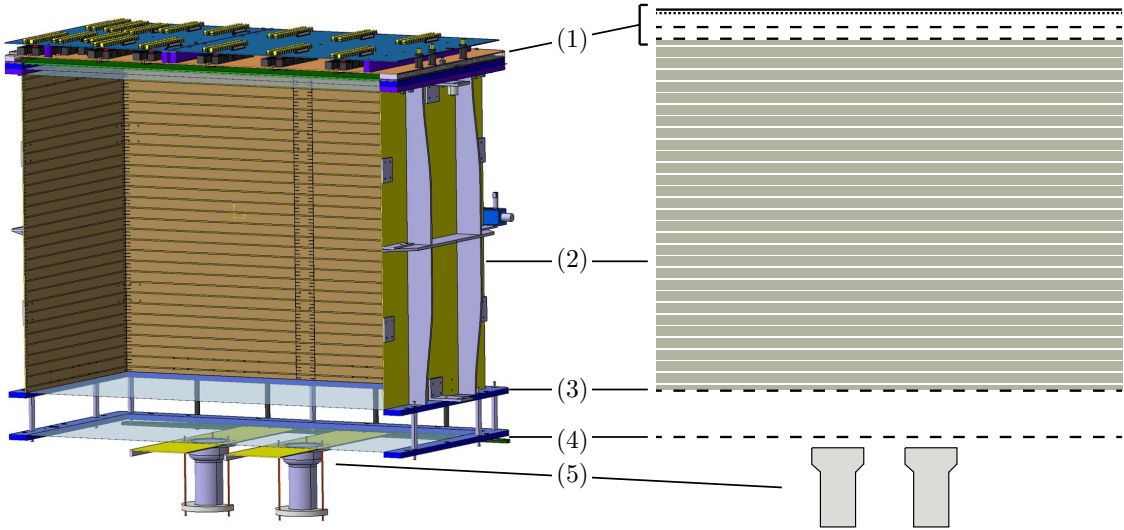


**Figure 3.** CAD drawing showing a cut through the LEM TPC and the detector layout: the charge readout sandwich (1) embedding extraction grids, LEM and 2D anode on top, the PCB drift box with printed copper strips (2) below, delimited on the bottom by the cathode grid (3) and an additional grid (4) to protect the two PMTs (5) from cathode discharges.

ground point of the multiplier is connected to the extraction grid in liquid, all the multiplication stages to the corresponding field shaping electrodes, finally the DC output (the last stage) to the cathode. The last stages are connected to the respective electrodes through  $20\text{ M}\Omega$  resistors that limit the current in case the cathode grid discharges to the wall of the cryostat. The maximum achieved drift field was  $1\text{ kV/cm}$ , with  $60\text{ kV}$  output voltage on the cathode. The potential of all the stages can be globally shifted by a DC voltage, in order to match the needed voltage on the extraction grid in liquid without affecting the drift field. Four capacitive level meters are installed around the charge readout sandwich on top of the detector. The measurement of the liquid level in different positions allows to adjust the detector with respect to the liquid level. In fact, the entire vessel can be tilted by means of screw driven movable stands.

## 2.2 The charge readout sandwich

The readout sandwich, shown schematically in Figure 4, consists of the two extraction grids, the LEM, the 2D projective readout anode, the spacers and the signal routing PCBs. The design parameters of the LEM are the same as the  $10 \times 10\text{ cm}^2$  prototype operated in a 3 lt detector [5], and the same applies for the 2D anode.

The  $1\text{ mm}$  thick LEM has an active area of  $40 \times 76\text{ cm}^2$  with about  $5 \times 10^5$  holes drilled. To limit the charge involved during a discharge, the LEM electrodes are divided in eight sectors along the long side and powered through  $500\text{ M}\Omega$  resistors. When a spark occurs, only the affected sector is discharged, because the distance between the electrodes of two sectors ( $1.6\text{ mm}$ ) is enough to avoid the propagation of the discharge from one sector to the other. The LEM was produced by a

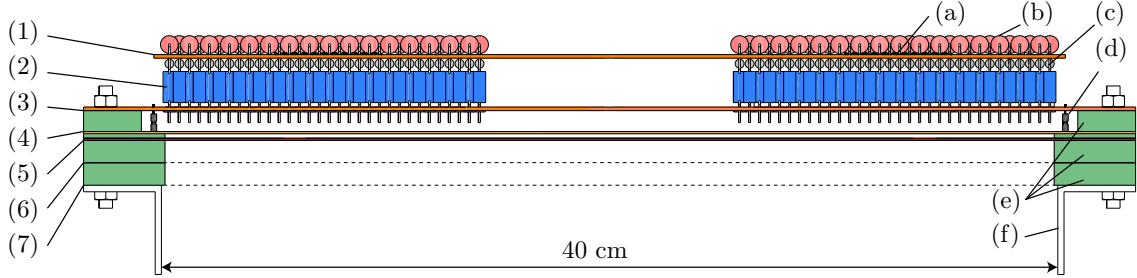


**Figure 4.** 2D CAD drawing of the readout sandwich, providing charge extraction, amplification and detection. The main elements are listed on the left (numbers): the signal distribution PCB plane (1), the HV decoupling capacitors (2), the HV distribution PCB plane (3), 2D anode (4), LEM (5), extraction grid in gas (6) and in liquid (7). Other components shown in the graphics (letters) are the connectors for the signal cables (a) behind the surge arresters (b), 33  $\Omega$  resistors (c), the multi pin connectors between the anode and the HV distribution plane (d), epoxy frames and spacers (e) and finally supporting angles to attach the sandwich to the drift volume (f).

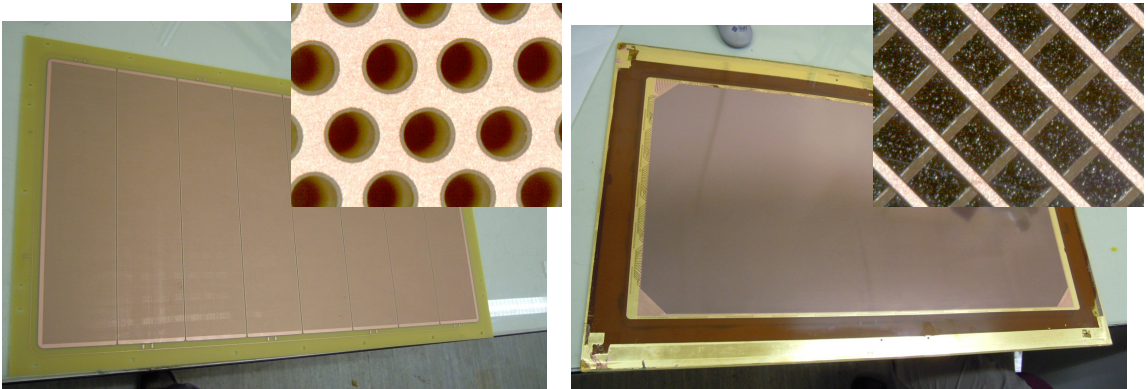


**Figure 5.** Picture of the  $76 \times 40 \text{ cm}^2$  LEM with close-up of its holes (left) and picture of the 2D anode with close-up of its strips (right).

company specialised in PCB manufacturing<sup>3</sup>. In order to maximise the amplification gain, 40  $\mu\text{m}$  thick dielectric rims were chemically etched [5]. To prevent the surface from corrosion, the metal electrodes were passivated. A picture of the LEM with a closeup of the holes is shown in Figure 5. To maintain a uniform distance from the anode, a 2 mm thick spacer is installed in between the top LEM face and the anode strips. Its shape matches the division in sectors of the LEM in order not to introduce additional dead space. The same structure is installed below the LEM to reduce the sagging due to its weight.

The anode, produced at the CERN TS/DEM workshop, has the same active area as the LEM and 256 channels per view, but is not subdivided into sectors. In view of a possible test beam, in order not to have any strip parallel to the incoming particles, the strips are rotated by 45° with respect to the long anode side. Pictures of the anode and a close view of the strips are shown in Figure 5.

The two extraction grids, with a distance of 1 cm from each other, are mounted 1.2 cm be-

<sup>3</sup>Eltos S.p.A., San Zeno (AR) Italy.



**Figure 6.** Pictures of the details of the detector: one of the extraction grids (left) and the charge readout sandwich during the assembling (right): the half in the back is already covered with the signal plane, in the foreground the HV distribution plane with the decoupling capacitors and the  $500\text{ M}\Omega$  resistors is seen.

low the LEM. Built with the same technique as the cathode and the PMT protecting grid, they are made of  $150\text{ }\mu\text{m}$  thick stainless steel foils chemically etched, to leave a square grid with a pitch of  $3\text{ mm}$  and  $150\text{ }\mu\text{m}$  thick *wires*. A picture of the grid is shown on the left of Figure 6. They are glued to  $1\text{ cm}$  thick PCB frames, that provide the right tension to keep them flat. For construction constraints, instead of stretching the grid, the frame was compressed during the gluing phase. The alignment between the two grids is within a wire diameter in the center, but it becomes worse at the edges, because the two grids are inevitably stretched slightly differently. Potentially, this can compromise the grid transparency, that can be restored increasing the field between the top extraction grid and the bottom LEM electrode. Image distortions can be caused by the field configuration around the extraction grids, and for this reason the pitch of the grids was chosen to be equal to the readout strip pitch.

The top part of the charge readout sandwich, shown on the right of Figure 6, hosts the components to feed the bias voltages, to decouple the signal from the high voltage and to protect the electronics from discharges. As displayed in the scheme of Figure 7, each electrode is connected independently via SHV feedthrough and a low pass filter to a separate channel of the power supply. This configuration allows to apply arbitrary field configurations. In order to be able to operate the anode at positive voltages, each of the 512 readout strips is connected via  $500\text{ M}\Omega$  resistors to the guard ring of the anode. They are mounted on a first *signal routing plane*, which is positioned on top of the anode. The  $270\text{ pF}$  HV decoupling capacitors connect this first plane to a second one, where a discharge protection circuit is installed as well as the connectors for the sixteen signal cables. Finally, the signal cables are fed through the cryostat and connected to the charge acquisition system. Both the discharge protection circuit as well as the readout electronics and acquisition system are detailed in the following section.

### 3. Readout electronics

A general LAr TPC acquisition layout for charge and light is presented in Figure 8. Both acquisition systems can be triggered by the prompt scintillation light detected with an array of PMTs immersed

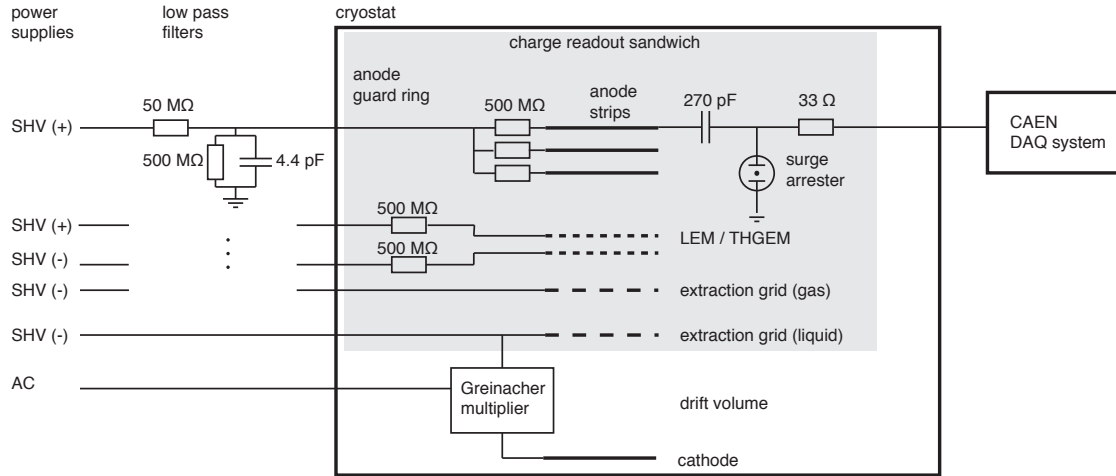


**Figure 7.** Electrical scheme of the TPC with the HV connections on the left and the data acquisition system on the right. The gray box shows the components which are embedded in the charge readout sandwich.

in LAr. For the acquisition of the light signals, commercially available digitizers, such as the 250 MHz V1720 from CAEN<sup>4</sup> can be used. In order to acquire the charge data, we developed, in collaboration with CAEN, a new charge acquisition system. We chose a scalable and compact design, which could be used for detectors up to one ton scale with  $O(1000)$  readout channels. As shown in Figure 8, charge sensitive preamplifiers, ADCs and acquisition logic are placed on a single board. The purpose of the system is to continuously acquire simultaneously the waveform of each readout channel, maintaining a precise time synchronisation between different channels. In addition we implemented programmable triggers, based on the ionisation charge digitised signals. We also chose to have preamplifiers directly pluggable (and thus exchangeable) on the acquisition boards, to be optimised to the needs of specific detectors. In our case we have developed custom made preamplifiers for unipolar charge collection signals, with sensitivities down to a few thousand electrons.

### 3.1 Design requirements

The final goal of a LAr TPC detector is to allow the 3D reconstruction of an ionising particle trajectory crossing the LAr volume and the determination of the produced ionisation charge along its path. Starting from the basic interaction of a charged particle with LAr, ionisation charge is produced as well as scintillation light (128 nm), which can be detected with cryogenic PMTs coated with TPB wavelength shifter [11]. The ionisation electrons, under the action of electric fields typically between 500 V/cm and 1000 V/cm, are drifted with a speed between 1.6 mm/ $\mu$ s and 2 mm/ $\mu$ s towards the liquid surface [13]. Finally in a LEM-TPC, after extraction into the gas phase and amplification inside the LEM holes, the electrons are collected on the electrode strips of a 2D anode, which are read out using low-noise charge preamplifiers.

We have already shown in [5] that effective gains of about 30 are achievable in stable, long-term conditions. The effective gain is defined as the ratio of the effectively collected charge on

<sup>4</sup>CAEN S.p.A., <http://www.caen.it>.

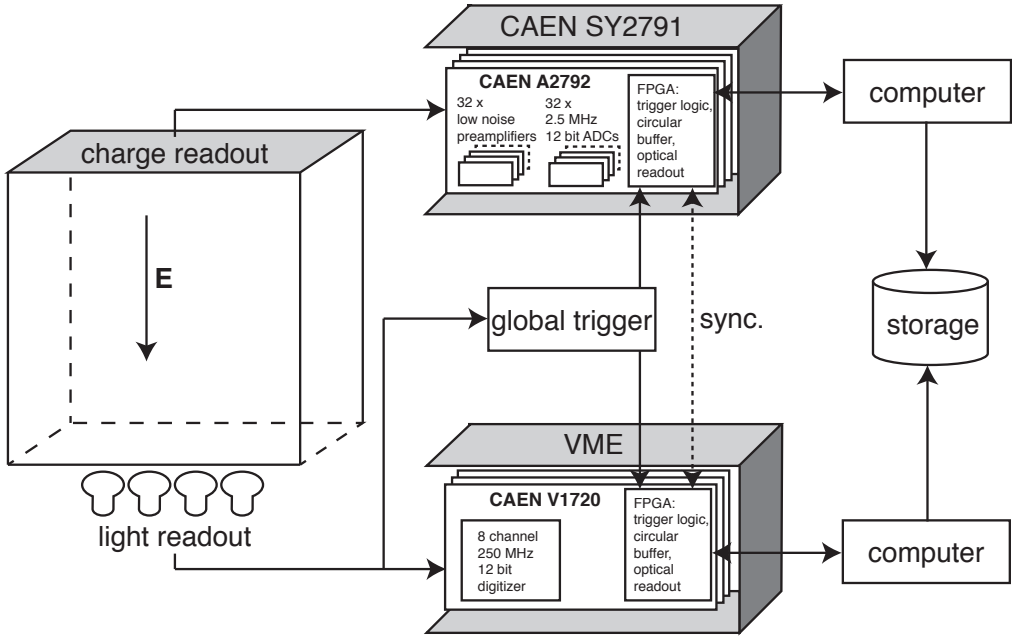


**Figure 8.** Schematic diagram of charge and light readout organisation of a LAr-TPC.

the readout electrodes compared to the one deposited in the liquid argon medium, however correcting for potential charge losses due to impurity attachment. The anode consists of two sets of perpendicular readout strips ( $x$  and  $y$  coordinate), designed such that each set collects about half of the incoming charge. Taking into account that the pitch of the LEM holes is  $O(1\text{ mm})$ , the pitch of the readout strips is set to 3 mm. The drift coordinate  $z$  can be directly obtained by measuring the time difference between the prompt scintillation light used as a trigger of the event and the collection time of the charge. The charge acquisition system has to be able to continuously acquire simultaneously the waveform of each readout channel with a precise time synchronisation, over an acquisition window lasting longer than the maximal drift time (typically  $O(\text{ms})$ ). In addition the system has to be compact in order to be placed as close as possible to the detector. Even with signal cables as short as possible, the capacitance at the input of the charge sensitive preamplifier in our setup is about 200 pF. The mean charge per readout strip in our anode, deposited by a minimum ionising particle (MIP) parallel to the readout plane and perpendicular to the readout strips, is  $\sim 1.5\text{ fC}/\text{strip}$  without gain from the LEM. For the design of our charge sensitive preamplifier, we hence required a signal to noise ratio of  $>15$  for 1.5 fC input charge and a combined detector and cable capacitance of about 200 pF. With a preamplifier sensitivity of about 10 mV/fC and a 12 bit ADC with a full range of 3.3 V, the RMS noise is comparable with the least significant bit of the ADC.

In order to achieve the low noise requirements, a first charge integrating stage is followed by a signal shaper, consisting of an integrator and a differentiator. In order to obtain a reconstruction precision of about 1 mm for the  $z$ -coordinate, a fast signal rise time of about 0.5  $\mu\text{s}$  combined with a sampling rate of about 2 MHz are required. For the falling time constant, a few microseconds is an acceptable compromise between the signal to noise requirement and the double track resolution.

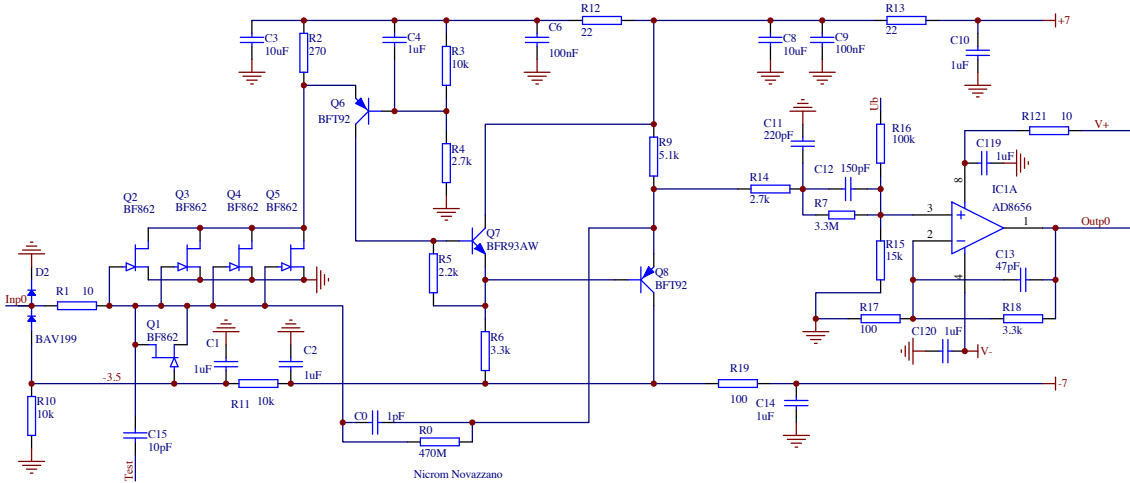


**Figure 9.** Schematic diagram of the charge sensitive preamplifier.

### 3.2 Charge sensitive preamplifiers

In this section we first describe the custom design of our front-end charge preamplifier specially optimised for our detector, then we present its performance in terms of pulse shaping and noise characterisation for different input capacities.

The basic layout, shown in Figure 9, consists of a protection circuit at the input, a charge amplifier and a shaper followed by a non-inverting linear amplifier. The circuit of the principal charge-amplifier loop with four NPX BF862 JFETs at the input is based on a preamplifier design for high-capacitance silicon detectors [14]. For the RC feedback we have chosen a 1 pF capacitor  $C_0$  which is discharged through a resistor  $R_0$  with a time constant  $\tau_F = 470 \mu\text{s}$ . The shaping of the signal is then done with a RC-CR configuration which includes a mechanism to suppress the undershoot caused by the feedback RC: the resistor  $R_7$  is chosen such that the product with the parallel capacitance  $C_{12}$  approaches  $\tau_F$ . If they are well matched, the zero pole caused by the feedback time constant is cancelled. The final transfer function of amplifying loop and RC-CR shaper is given by the equation [15]:

$$H(\omega) \propto \frac{\omega}{(i\omega\tau_D + 1)(i\omega\tau_I + 1)}, \quad (3.1)$$

with the computed values for the time constants  $\tau_I = 0.48 \mu\text{s}$  and  $\tau_D \approx 2.75 \mu\text{s}$ . After the shaping, the required voltage sensitivity of about 10 mV/fC is reached by means of an operational amplifier<sup>5</sup> in a non-inverting configuration with a set gain of 30. Figure 10 shows the realisation of two preamplifier circuits with discrete components on a PCB layout with four layers. The preamplifier response function was then explicitly derived from Equation (3.1) with an additional low pass filter (time constant  $\approx \tau_I$ ) coming from the non-inverting operational amplifier loop after the shaper. The

<sup>5</sup>AD8656 operational amplifier, Analog devices, <http://www.analog.com>

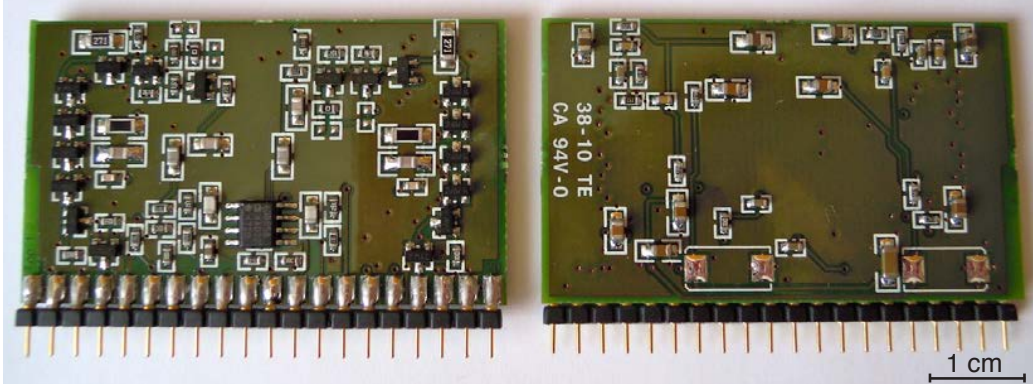


**Figure 10.** Photograph of two preamplifier circuits realized with discrete components on a four layer PCB.

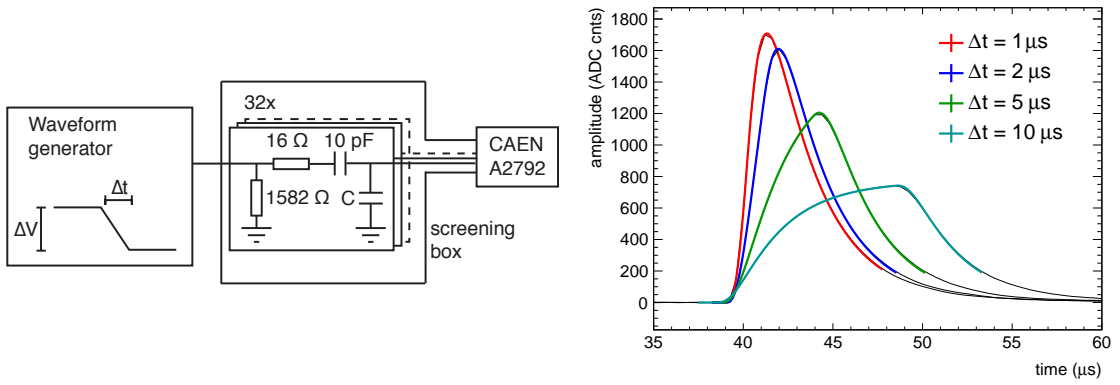


**Figure 11.** Left: electric scheme of the test setup for the performance measurements of 32 preamplifiers. Right: preamplifier response data (black) of a charge injection with different time intervals from  $1 \mu\text{s}$  to  $20 \mu\text{s}$  superimposed with the corresponding fits (colored curves). [See text for details].

resulting response function is given by [15]:

$$V_{\text{response}}(t) = I \frac{e^{t/\tau_D} \tau_D - e^{t/\tau_I} (\tau_D + t \frac{\tau_D - \tau_I}{\tau_I})}{(\tau_D - \tau_I)^2}. \quad (3.2)$$

The performance of 32 preamplifiers was tested with the setup presented in Figure 11. It allows to simultaneously feed with a well defined test charge 32 preamplifiers, housed on a CAEN A2792 acquisition board (see Section 3.3). A factor 1/100 attenuator as well as  $10 \pm 0.25 \text{ pF}$  test capacitors and additional input capacities  $C$ , to simulate different detector and cable capacitances, are inside a screened box. The trapezoidal voltage pulse shown in Figure 11 allows to input a constant current with different durations  $\Delta t$  to each preamplifier. The voltage step  $\Delta V$  was measured with a Keithley 2000 Multimeter<sup>6</sup>.

The signals shown in Figure 11 were obtained by pulsing the test capacitor with a constant voltage step  $\Delta V$ , but with different duration  $\Delta t$ , thus keeping the injected charge constant. The fitted preamplifier response, convoluted with a constant current over a time  $\Delta t$ , is superimposed

<sup>6</sup>Keithley Instruments Inc., <http://www.Keithley.com>.

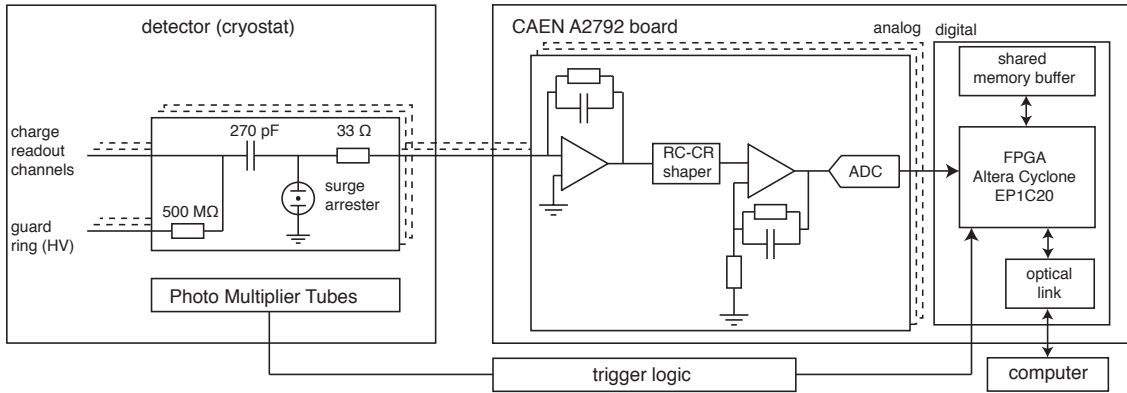


**Figure 12.** Overall layout of the setup with the detector on the left and the readout electronics on the right.

in colour in Figure 11 to the digitised waveforms. The resulting time constants, given in Table 1, agree well with the computed values.

Besides the signal shape, we have investigated the voltage sensitivity and linearity by measuring the signal amplitude for input charges in the range from 10 fC to 180 fC. For these measurements, a very short pulse width of  $\Delta t = 0.1 \mu\text{s}$  was chosen. A summary of the performance measurements of 32 different preamplifiers is given in Table 1. The RMS value of the intrinsic equivalent input noise charge (ENC) was measured with four different test capacities  $C$  at the input of the preamplifiers.

**Table 1.** Average parameters measured with 32 different preamplifiers. The given error equals the observed spread.

shaping time $\tau_D$	$2.8 \pm 0.1 \mu\text{s}$
shaping time $\tau_I$	$0.45 \pm 0.02 \mu\text{s}$
sensitivity	$13.8 \pm 0.4 \text{ mV/fC}$
open loop gain	$\approx 10^4$
linearity (0-180 fC)	$\pm 1\%$
ENC in RMS: $C = 10 \text{ pF}$	$470 \pm 30 e^-$
$C = 92 \text{ pF}$	$580 \pm 30 e^-$
$C = 210 \text{ pF}$	$770 \pm 30 e^-$
$C = 480 \text{ pF}$	$1420 \pm 30 e^-$

### 3.3 Data acquisition system

The overall setup shown schematically in Figure 12, can be divided in two parts: the detector and the electronics readout crates. Starting from the electrodes of the 2D anode which are usually kept at HV to optimize the charge collection, the signals are first decoupled with 270 pF HV capacitors<sup>7</sup>. Since the LEM is operated in pure argon gas, it may occur that occasionally electron avalanches inside the LEM holes turn into streamers which short the two LEM electrodes, finally inducing a

<sup>7</sup>Kekon HV capacitors, 270 pF, 10 kV, NP0, <http://www.kekcon.com>

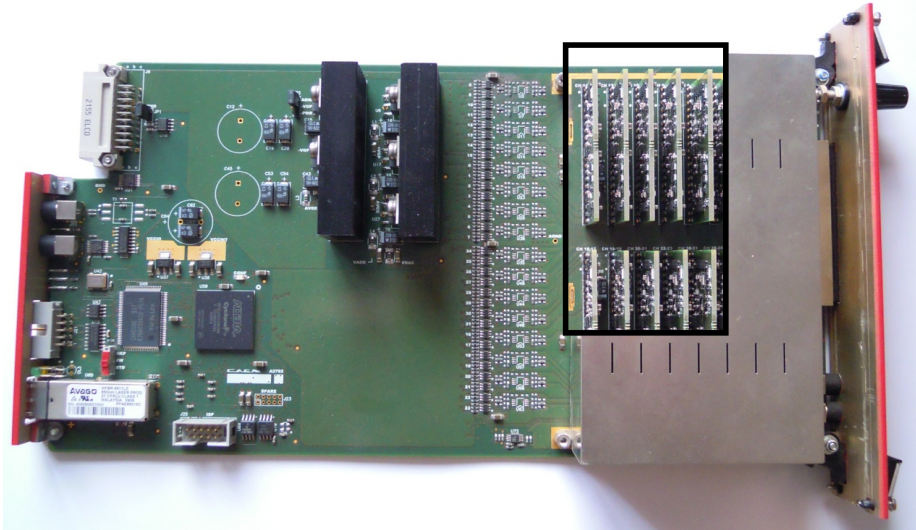


**Figure 13.** Picture of a CAEN A2792 readout board. The window on the right shows the plugged preamplifier circuits below the screen.

discharge on the anode. A multiple stage discharge protection was implemented to avoid damage to the electronics: as first stage, surge arresters<sup>8</sup>, mounted close to the decoupling capacitors inside the detector, open to ground when voltages exceed  $\sim 90$  V; low leakage double diodes<sup>9</sup>, followed by a  $10\Omega$  resistor, and a JFET are directly implemented on the preamplifier circuit as shown in Figure 10. The readout system consists of several CAEN SY2791 crates designed and built for this project in collaboration with CAEN, each hosting a linear regulated power supply and 8 CAEN A2792 32 channels readout boards. Detector and readout system are interconnected with a 32 signal shielded flat cable. The preamplifiers (see Figure 10) are directly plugged on the A2792 boards, as shown in Figure 13. In order to reduce pickup noise the preamplifiers are fully surrounded by a screen connected to ground. A relevant feature of the design is that the readout boards contain both the analog and the digital sections, as illustrated on the right part of Figure 12. Signals are first amplified, shaped and then digitised by individual 12 bit 2.5 MS/s ADCs with serial readout interface. The 32 digitised signals are further processed by an FPGA, that continually stores the data in 1 MB circular memory buffers for each channel independently, it provides the trigger logic and controls the transfer of the data to a computer via an optical link. The time synchronisation between different boards and different crates is done with a single wire connection (TT-link) in a daisy-chain configuration. In addition to the clock signal, which is provided by the master board of a crate, also commands like *start*, *stop* and *trigger alert* are propagated through the TT-link. The system provides a sophisticated channel by channel trigger with two programmable thresholds: in case the signal exceeds a threshold value on any channel, a trigger alert signal is forwarded via the TT-link to all the other channels, causing them to lower the threshold to a second predefined value. Alternatively, the acquisition can also be triggered globally with an external signal. Such a trigger can for example be generated by the prompt scintillation light detection.

<sup>8</sup>EC 90, EPCOS AG, Munich, Germany

<sup>9</sup>BAV199 from NPX

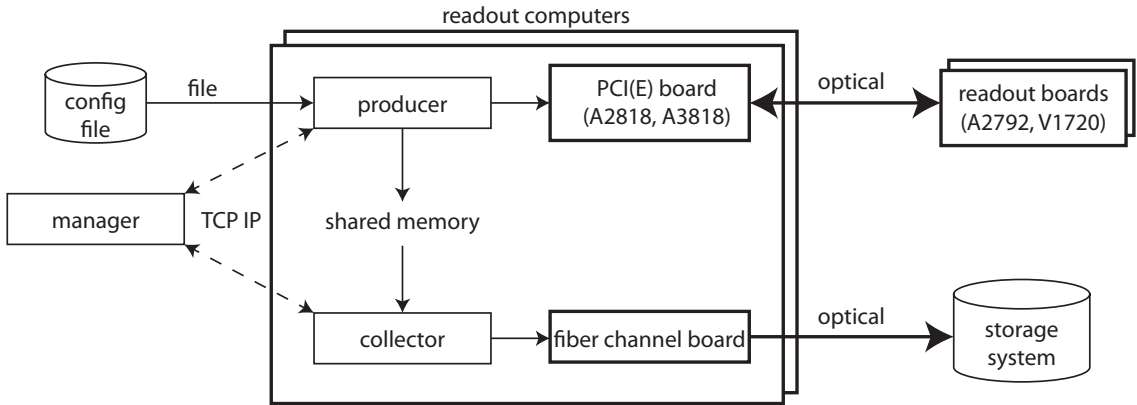


**Figure 14.** Schematics of the data acquisition system.

Figure 14 shows the schematics of the data acquisition system. The optical readout link can connect up to eight A2792 to a CAEN A2818 (PCI) or A3818 (PCIE) card on a computer.

The data acquisition system is based on commercial Linux PCs. In order to increase the data throughput, different crates can be connected to different computers. On each readout computer two programs are running in parallel, the *producer* and the *collector*. The *producer* task is to send commands to the readout boards and to read the data from each board in event blocks. This data are then directly written to the *shared memory*. The *collector* reads from the shared memory and writes data to a file on an external storage disk. All programs (*producer* and *collector*) running on different readout computers are controlled by a user interface (*manager*). It allows the user to load a configuration and to start and stop the acquisition.

## 4. First operation and performance of the LEM-TPC

### 4.1 Detector commissioning and operation

The filling of the detector vessel can be subdivided into three phases: first, the main vessel volume containing the detector was evacuated down to about  $10^{-5}$  mbar in order to let the materials outgas (the observed rate of outgassing was estimated to be  $10^{-3}$  mbar l/s). Next, after adding 1 bar of pure argon gas, the gas recirculation was turned on, efficiently further removing outgassed molecules. At this stage, the purity in the warm gas is on the order of 100 *ppb*. At the same time the external bath was filled with LAr, cooling down the detector. Once the system was in thermal equilibrium, the cryostat could be filled with liquid argon obtained commercially which typically contained *ppm* impurities of oxygen and other elements. In order to reach liquid argon impurity concentrations at the level of *ppb*, the liquid was passed through a custom made purification cartridge which contains a stack of reduced CuO powder and 3 Å molecular sieve<sup>10</sup>. After precise adjustment of the LAr level in the middle of the two extraction grids, we have operated the detector during about four weeks, starting with the commissioning of the Greinacher circuit, the purification system and finally also the LEM-TPC.

<sup>10</sup>Zeochem Z3-01, <http://www.zeochem.ch>.

	dimension	electric field
anode-LEM	0.2 cm	2 kV/cm
LEM	0.1 cm	30–35 kV/cm
grid-LEM	1.2 cm	0.6 kV/cm
extraction	1.0 cm	2 kV/cm (in LAr)
drift	60 cm	0.4 kV/cm

**Table 2.** Nominal electric field configuration and dimensions of the LEM-TPC. The absolute potential of the anode was kept at +1 kV.

The signals of the detector were read out with the acquisition system described in Section 3.3. The 2D anode with  $2 \times 256$  readout strips required the use of two fully equipped CAEN SY2791 crates. It was globally triggered by the prompt scintillation light, measured with the two cryogenic PMTs positioned below the cathode grid of the detector. With a 20 Hz trigger rate we achieved a stable data throughput of about 40 MB/s.

Stable operation of the detector was reached with the nominal electric fields reported in Table 2. Figure 15 shows four typical cosmic ray events, taken from the highest gain run with an amplification field of 35 kV/cm. From top to bottom, there are two cosmic muons crossing the detector, a deep inelastic interaction and an electromagnetic shower candidate. These plots show the usual representation of events with the drift time as a function of the strip number for both views. The greyscale represents the signal amplitude for each sample in a linear scale. It can clearly be seen that both views show symmetric unipolar signals which are clearly distinguishable from the noise. As a consequence of the good signal to noise ratio and the spatial resolution, small structures like knock-on electrons – also called  $\delta$ -rays – can be identified and reconstructed in three dimensions as demonstrated below. Since cosmic muons produce straight crossing tracks and the energy deposition is known to be  $\sim 2.1$  MeV/cm, the events can be used to characterise the detector in terms of free electron lifetime and amplification. An obvious limitation of this charge readout was the inactive area introduced by the segmentation of the LEM. The 1.6 mm wide gaps between the LEM electrode segments appear as equally spaced missing charge, as seen in the two muon events in Figure 15.

## 4.2 Event reconstruction

The event reconstruction of the digitised raw waveforms was done with the so-called Qscan software package for LAr detectors [16]. Here we give a brief description of the basic steps in the reconstruction procedure. A more detailed description of the event reconstruction in a LAr-TPC can be found elsewhere [15, 16]. Due to the presence of coherent pick up noise at our laboratory location, which could not be eliminated during the run, the events had to be digitally filtered. As explained in Ref. [5], an algorithm to subtract common noise on all channels has been applied. This algorithm basically makes use of the fact that the same coherent noise is picked up by all the electrodes and subtracts it. In addition, remaining discrete noise frequencies, which appeared dominantly on all the channels in the power spectrum, have been suppressed. Finally, a pedestal value, which is computed as the average amplitude in the pre-trigger window from 0 to 56  $\mu$ s, is subtracted from each waveform.

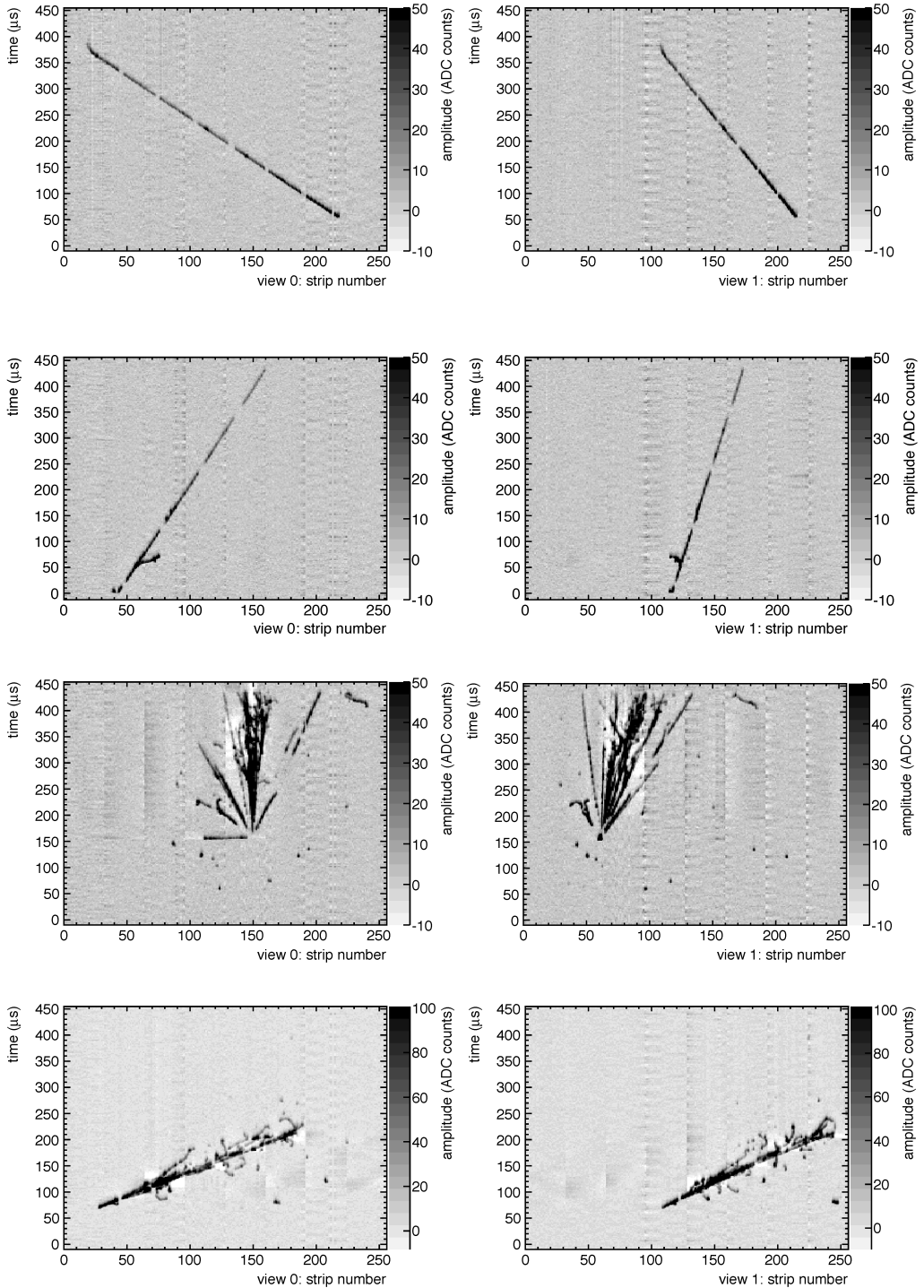


**Figure 15.** Cosmic ray event displays (left: view 0, right view 1), recorded in double phase conditions with a LEM field of 35 kV/cm. The four event displays show from top to bottom two muons, a hadronic and an electromagnetic shower candidate. [See text for more details.]

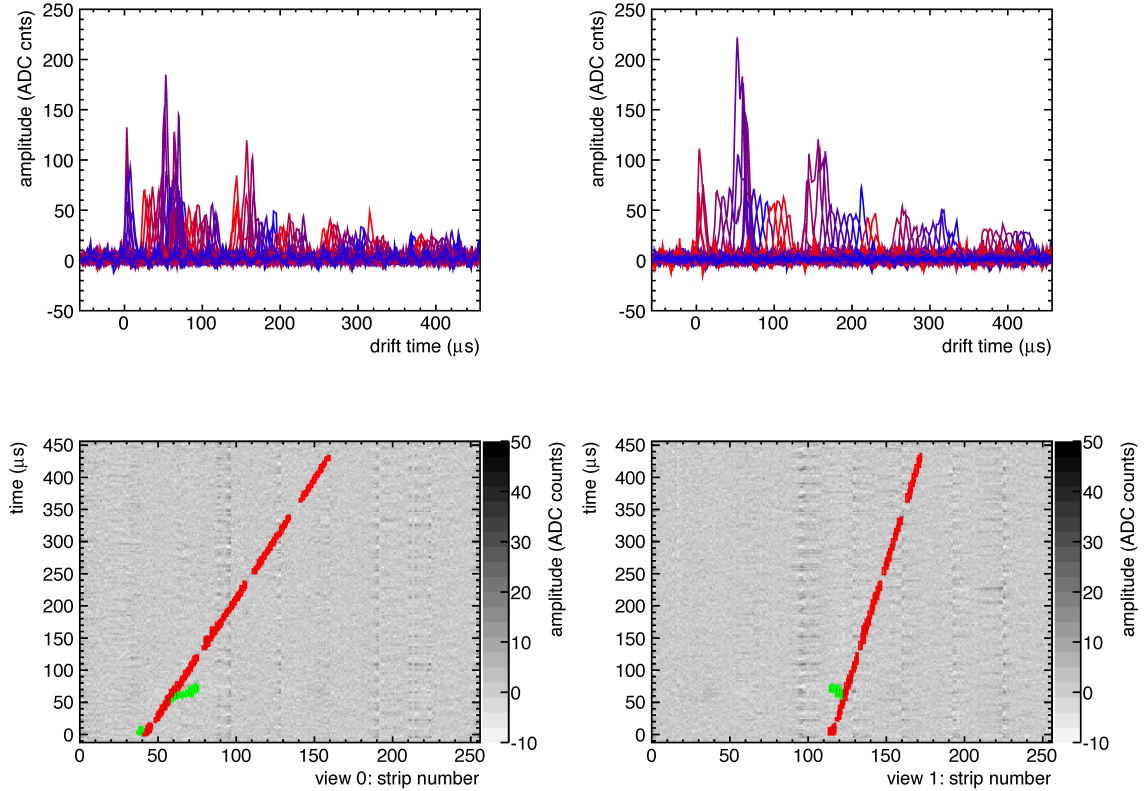


**Figure 16.** Typical cosmic muon crossing the full drift length of 60 cm. Top: signal waveforms of all the channels of the two views; bottom: event display representation of the same event showing drift time versus anode strip number. Found hits of the main  $\mu$  track are marked in red, identified  $\delta$ -ray hits are marked in green.

After the digital signal processing of the waveforms the so called hit-finding algorithm discriminates physical signals from noise. The physical parameters which can be extracted from found hits are the time when the signal rises and the hit integral. Since the events are always triggered by the prompt scintillation light, the signal time is equal to the drift time of the charge. The methods to extract the drift velocity and its uniformity has been reported elsewhere [8] and found to be consistent with  $v_d \sim 1.4 \text{ mm}/\mu\text{s}$ . The hit integral, after calibration, is a direct measurement of the ionisation charge  $\Delta Q$ . After clustering adjacent hits, straight tracks have to be found and reconstructed. This is done by converting the hit parameters from the real space (strip and drift time) to the parameter space of straight lines. In the Hough space [17], lines appear as points, thus the problem of finding hits in a straight line is reduced to the problem of finding maxima in the parameter space of straight lines. Another advantage of the Hough algorithm is that it is not sensitive to missing hits due to the LEM segmentation, as discussed above. In the event display shown in Figure 16 all the hits which are identified as part of a straight line are marked in red. In order also to reconstruct  $\delta$ -rays with enough energy to produce secondary tracks (few MeV) an algorithm that searches for residual hits which are attached to but not part of the main muon track was implemented. If such an attachment

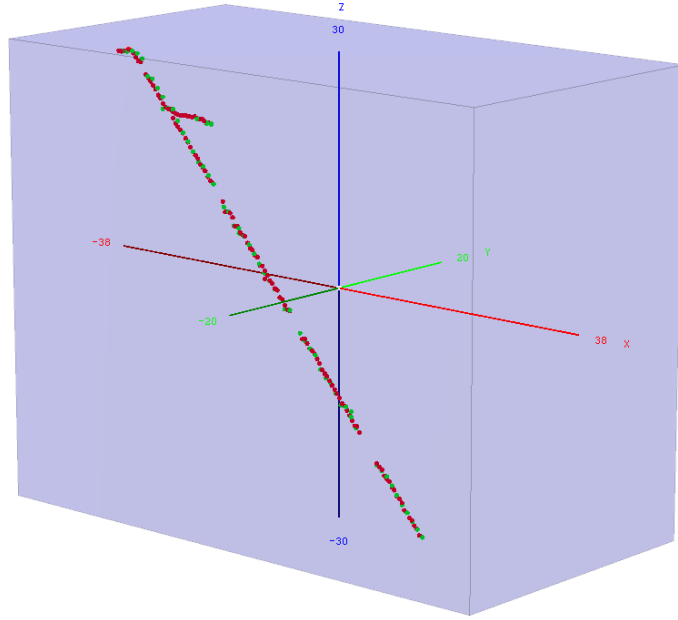


**Figure 17.** Crossing muon event with a  $\delta$ -ray reconstructed in three dimensions. Each dot corresponds to a three dimensional hit of the track. View 0 (1) hits are shown in red (green).

of the main track (green) consists of at least two hits, it is identified as  $\delta$ -ray.

After matching two main tracks with equal time endpoints, the three dimensional coordinates of its hits can easily be computed as well as the three dimensional track pitch  $\Delta x$  of each hit. Together with the information of its charge  $\Delta Q$  the charge per unit length  $\Delta Q/\Delta x \approx dQ/dx$  can be computed. Since  $\delta$ -rays are typically not straight as it is the case for the cosmic muons, each  $\delta$ -ray hit is matched by time with a  $\delta$ -ray hit of the second view. In case the  $\delta$ -ray appears only in one view, the hits are matched with the main muon track. Figure 17 shows a three-dimensionally reconstructed muon track with a  $\delta$ -ray.

#### 4.3 Free electron lifetime measurement

As described in Section 2 the cryogenic system was equipped with two separate purification systems. During the run period both systems were operated, thus it was important to monitor the liquid argon purity. In order to measure the charge attenuation as a function of the drift time, we have used the reconstructed cosmic muon tracks. The data points in Figure 18 show the mean  $dQ/dx$  values of all reconstructed muons for different drift times. It can be seen that the exponential function  $e^{-t_{drift}/\tau_e}$  with the free electron lifetime  $\tau_e$  perfectly fits the obtained distribution. The maximum electron drift time is about  $430 \mu\text{s}$ . The plot on the right side shows the lifetime evolution during the last three weeks of operation. Starting from a lifetime of about  $170 \mu\text{s}$  we first did initial tests with the liquid recirculation. During this commissioning period the free electron lifetime remained constant. In a second phase, the gas recirculation was turned on. Due to changes in pressure and liquid argon level we did not acquire data with the double phase readout. However, after stopping the gas recirculation, the measured free electron lifetime was not significantly improved although

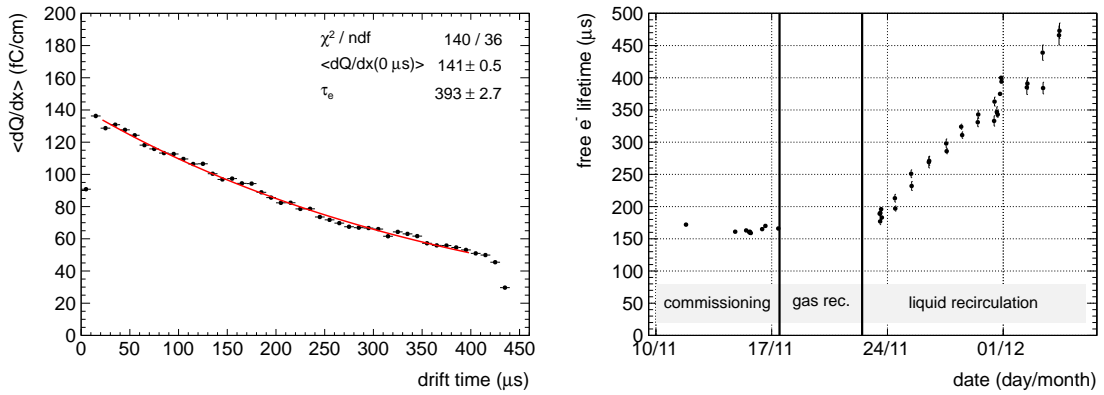


**Figure 18.** Left:  $\langle dQ/dx \rangle$  as a function of the drift time superimposed with an exponential function with the decay time constant  $\tau_e = 393 \pm 3 \mu\text{s}$  fitted to the data points. Right: evolution of the free electron lifetime during the run period.

was maintained at constant value. During the last phase we have operated the liquid argon recirculation system at a flow rate of about 5 to 7 lt LAr/h. Since we saw a steady increase of the free electron lifetime until we stopped the run, we conclude that the liquid argon recirculation system was efficiently working. When we stopped the run a lifetime of  $470 \mu\text{s}$  was measured. This corresponds to an oxygen equivalent impurity concentration of about 0.64 ppb.

#### 4.4 Amplification gain and energy spectrum of $\delta$ -rays

After the determination of the free electron lifetime, the factor  $e^{t_{drift}/\tau_e}$  has to be used to correct for charge losses due to the electron attachment to impurities. This allows then to do a measurement of the effective gain and the signal to noise ratio for the recorded MIP events. As explained in detail in reference [5] the effective gain of the device is defined as the ratio of the measured charge collected (and corrected for the measured electron lifetime) on both views  $\langle dQ_0/dx \rangle + \langle dQ_1/dx \rangle$  and the initially produced charge  $\langle dQ/dx \rangle_{MIP} = 10 \text{ fC/cm}$ . This means that this factor includes the intrinsic Townsend avalanche as well as losses at the liquid-gas interface, at the top extraction grid and at the LEM. The two plots in Figure 19 show the  $dQ/dx$  distributions for view 0 and view 1 from the run with  $35 \text{ kV/cm}$  amplification field, superimposed with a fitted Landau convoluted with a Gaussian. Besides the effective gain measurements it was important to verify that the strips of each view collect the same amount of charge. We use the measured  $dQ/dx$  distributions of both views to compute the asymmetry factor

$$\frac{\langle dQ_1/dx \rangle - \langle dQ_0/dx \rangle}{\langle dQ_1/dx \rangle + \langle dQ_0/dx \rangle} \approx 7\%. \quad (4.1)$$

In addition to a gain of 14 and a good sharing of the charge among the two views, we also measured an excellent signal to noise ratio of about 30 for a MIP. To compute this ratio, we used the mean amplitude of cosmic muon induced signals divided by the average noise, defined as the average RMS value for all the readout channels.

Figure 20 shows a summary of the effective gains obtained with different amplification fields between  $33 \text{ kV/cm}$  and  $35 \text{ kV/cm}$ . The values of all the other fields, defined in Table 2, were kept constant.

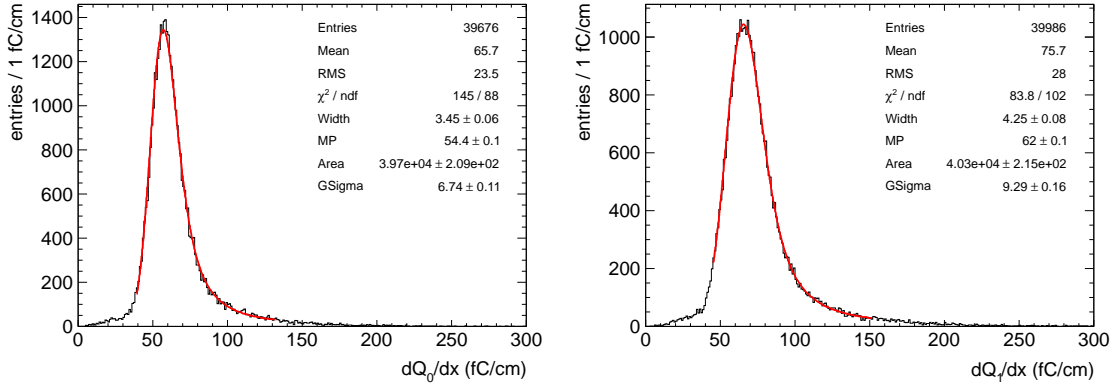


**Figure 19.**  $dQ/dx$  distribution for both views for selected straight tracks from a run with an amplification field of 3.5 kV across 1 mm. A Landau function, convoluted with a Gaussian is fitted to the distributions.

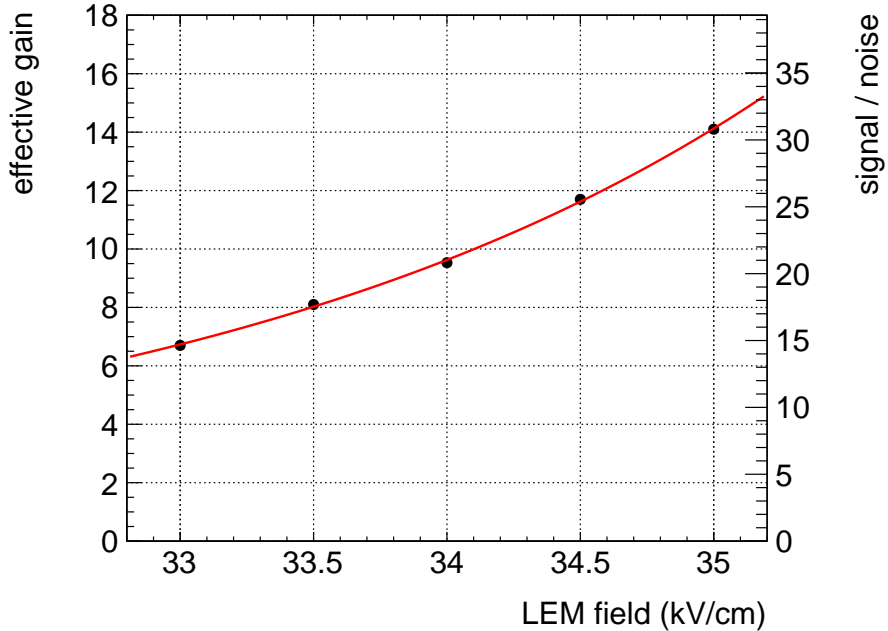


**Figure 20.** Effective gain of the detector (left) as a function of the LEM amplification field.

Figure 21 shows the number of reconstructed  $\delta$ -rays, normalised by the muon track length, as a function of the reconstructed kinetic energy. To get an estimation of the kinetic energy, the calorimetric approach of summing up the deposited energies of all the tagged hits was used. Since the initial part of the  $\delta$ -ray is less easily separated from the main muon track, the obtained kinetic energy is always an underestimation of the true value. In order to do a consistency check, Qscan has been interfaced with Geant 4 using the Virtual Monte Carlo package VMC [18]. Muons with a uniform distribution between 1 and 10 GeV/c and with the angular distribution of the observed cosmic rays were propagated in a simplified detector geometry, digitised and reconstructed, together with their  $\delta$ -rays. The obtained energy distribution of the MC generated  $\delta$ -rays is shown in Figure 21, above 3 MeV it agrees well with the data from cosmic rays. The theoretical curve

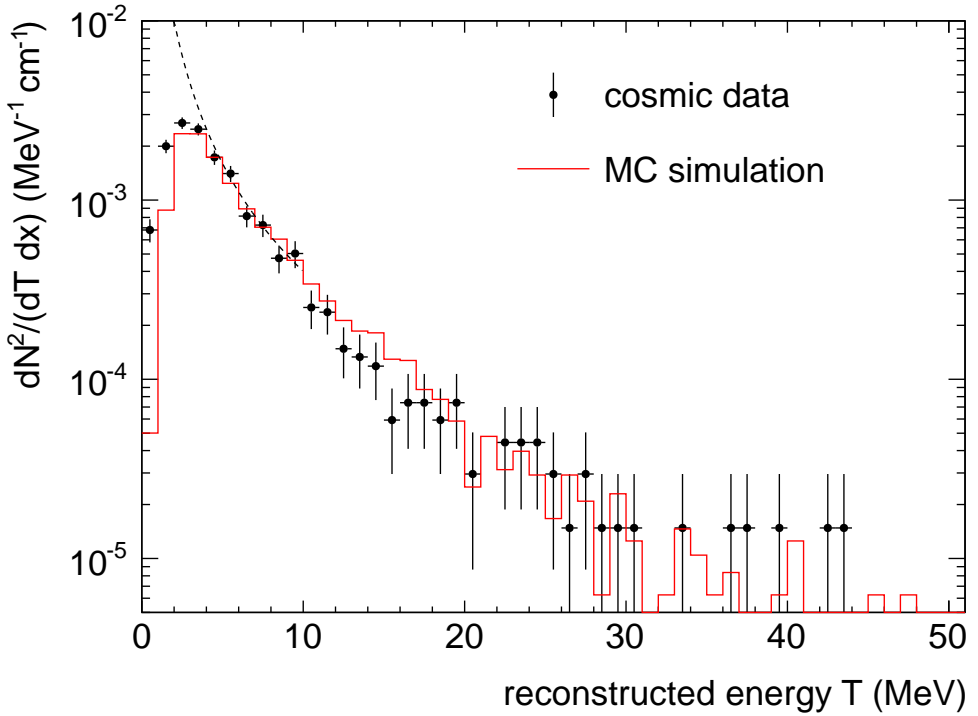


**Figure 21.** The reconstructed energy of  $\delta$ -rays that are longer than 0.5 cm from the collected cosmic muon sample, as well as from the MC generated muon events with a momentum uniformly distributed between 1 and 10 GeV/c.

$d^2N/(dT dx) \propto \beta^{-2} (1 - \beta^2 \frac{T}{T_{max}}) T^{-2}$ , where  $T$  is the kinetic energy of the  $\delta$ -ray,  $\beta$  its velocity, and  $T_{max}$  is defined in Ref. [19], is also shown as dashed line below 10 MeV, showing that with the present algorithm, the efficiency for reconstructing the  $\delta$ -rays drops below 5 MeV. The discrepancy between data and MC simulations below 3 MeV shows that the efficiency for reconstruction is slightly under-estimated in the simulation.

## 5. Conclusions

We have produced and successfully operated the largest LAr LEM-TPC with 2D readout anode of an area of  $40 \times 76 \text{ cm}^2$  ( $\sim 0.5 \text{ m}^2$ ) and 60 cm drift. During a very successful run with double phase ultra-pure argon at 87 K, the detector was exposed to cosmic rays and recorded a large number of events during a long-term data-taking period. A stable effective gain 14 was reached, giving an excellent signal to noise ratio of  $> 30$  for a MIP. The detector performance has been studied and a sample of  $\delta$ -rays was measured and compared to a MC simulation. The exact performance with a gain of  $\sim 30$  reached with the  $10 \times 10 \text{ cm}^2$  area chamber [5] could not be reproduced in this first test of a detector of  $\sim 0.5 \text{ m}^2$ -scale. The observed limitations such as this apparently lower maximum gain, the introduced dead space by the segmentation of the LEM, the large anode capacitance and the long signal cables, are presently being addressed and will be further treated and hopefully corrected in the near future.

## Acknowledgments

This work was supported by ETH Zurich and the Swiss National Science Foundation (SNF). We are grateful to CERN for their hospitality and thank R. Oliveira and the TS/DEM group, where several of the components of our detector were manufactured. We also thank the RD51 Collaboration for useful discussions and suggestions. Special thanks go to N. Bourgeois and the CERN PLC support group for the PLC system and to T. Schneider and Thin Film & Glass group of CERN for helping us for the WLS coating of the PMTs. We thank Maria de Prado (CIEMAT), Takasumi Maruyama (KEK/IPNS), Junji Naganoma (Waseda), Hayato Okamoto (Waseda) and A. Marchionni (FNAL) for their participation in the data-taking phase.

## References

- [1] S. Amerio *et al.*, “Design, construction and tests of the ICARUS T600 detector” *Nucl. Instrum. Meth. A* **527**, 329-410 (2004).
- [2] A. Rubbia, “Experiments for CP violation: A Giant liquid argon scintillation, Cerenkov and charge imaging experiment?,” [hep-ph/0402110].
- [3] A. Rubbia, “Underground Neutrino Detectors for Particle and Astroparticle Science: The Giant Liquid Argon Charge Imaging ExpeRiment (GLACIER),” *J. Phys. Conf. Ser.* **171**, 012020 (2009). [arXiv:0908.1286 [hep-ph]].
- [4] A. Badertscher *et al.*, “Giant Liquid Argon Observatory for Proton Decay, Neutrino Astrophysics and CP-violation in the Lepton Sector (GLACIER),” [arXiv:1001.0076 [physics.ins-det]].
- [5] A. Badertscher *et al.*, “First operation of a double phase LAr Large Electron Multiplier Time Projection Chamber with a 2D projective readout anode” *Nucl. Instrum. Meth. A* **641**, 48-57 (2011).
- [6] A. Badertscher, L. Knecht, M. Laffranchi, D. Lussi, A. Marchionni, G. Natterer, P. Otiougova and F. Resnati *et al.*, “Operation of a double-phase pure argon Large Electron Multiplier Time Projection Chamber: Comparison of single and double phase operation,” *Nucl. Instrum. Meth. A* **617**, 188 (2010) [arXiv:0907.2944 [physics.ins-det]].
- [7] A. Badertscher *et al.*, “Construction and operation of a Double Phase LAr Large Electron Multiplier Time Projection Chamber,” [arXiv:0811.3384 [physics.ins-det]].
- [8] A. Badertscher, A. Curioni, U. Degunda, L. Epprecht, A. Gendotti, S. Horikawa, L. Knecht and D. Lussi *et al.*, “First operation and drift field performance of a large area double phase LAr Electron Multiplier Time Projection Chamber with an immersed Greinacher high-voltage multiplier,” arXiv:1204.3530 [physics.ins-det].
- [9] A. Marchionni *et al.* [ArDM Collaboration], “ArDM: a ton-scale LAr detector for direct Dark Matter searches,” *J. Phys. Conf. Ser.* **308**, 012006 (2011) [arXiv:1012.5967 [physics.ins-det]].
- [10] A. Rubbia, “ArDM: A Ton-scale liquid Argon experiment for direct detection of dark matter in the universe,” *J. Phys. Conf. Ser.* **39**, 129 (2006) [hep-ph/0510320].
- [11] V. Boccone *et al.* [ArDM Collaboration], “Development of wavelength shifter coated reflectors for the ArDM argon dark matter detector,” *JINST* **4**, P06001 (2009) [arXiv:0904.0246 [physics.ins-det]].
- [12] S. Horikawa, A. Badertscher, L. Kaufmann, M. Laffranchi, A. Marchionni, M. Messina, G. Natterer and A. Rubbia, “Feasibility of high-voltage systems for a very long drift in liquid argon TPCs,” *J. Phys. Conf. Ser.* **308**, 012027 (2011) [arXiv:1009.4908 [physics.ins-det]].

- [13] W. Walkowiak, “Drift velocity of free electrons in liquid argon,” Nucl. Instrum. Meth. **A449**, 288-294 (2000).
- [14] C. Boiano *et al.*, “Wide-dynamic-range fast preamplifier for pulse shape analysis of signals from high-capacitance detectors”, IEEE Transactions on Nuclear Science 51 1931-1935 (2004).
- [15] D. Lussi, “Study of the response of the novel LAr LEM-TPC detector exposed to cosmic rays and a low momentum charged particle beam,” Ph.D. Thesis in Preparation, <http://e-collection.library.ethz.ch> (2013)
- [16] J. Rico, “First study of the stopping Muon sample with the ICARUS T600 detector,” Ph.D. Dissertation, ETH 14906, <http://e-collection.library.ethz.ch> (2002)
- [17] P. Hough, “Method and means for recognizing complex patterns”, U.S. Patent 3.069.654, Dec. 1962
- [18] I. Hrivnacova, “The Geant4 virtual Monte Carlo,” J. Phys. Conf. Ser. **119** (2008) 032025.
- [19] J. Beringer et al. (Particle Data Group), Phys. Rev. **D86**, 010001 (2012).